ARTICLE   OPEN

Check for updates

Efficient GW calculations in two dimensional materials through a stochastic integration of the screened potential

Alberto Guandalini [1,2 ✉], Pino D'Amico [1 ✉], Andrea Ferretti [1 ✉] and Daniele Varsano [1 ✉]

Many-body perturbation theory methods, such as the G_0W_0 approximation, are able to accurately predict quasiparticle (QP) properties of several classes of materials. However, the calculation of the QP band structure of two-dimensional (2D) semiconductors is known to require a very dense BZ sampling, due to the sharp q-dependence of the dielectric matrix in the long-wavelength limit ($\mathbf{q} \to 0$). In this work, we show how the convergence of the QP corrections of 2D semiconductors with respect to the BZ sampling can be drastically improved, by combining a Monte Carlo integration with an interpolation scheme able to represent the screened potential between the calculated grid points. The method has been validated by computing the band gap of three different prototype monolayer materials: a transition metal dichalcogenide (MoS_2), a wide band gap insulator (hBN) and an anisotropic semiconductor (phosphorene). The proposed scheme shows that the convergence of the gap for these three materials up to 50meV is achieved by using $\mathbf{k}$-point grids comparable to those needed by DFT calculations, while keeping the grid uniform.

INTRODUCTION

The GW approximation[1–4] is a well-established method for first principle calculations of electronic excitations of materials[5–7]. It provides access to quasi-particle energy bands as measured in ARPES experiments[8], satellites[9,10], lifetimes[11], and spectral functions[12,13]. Since its development, the GW approximation has been applied to a large class of systems ranging from bulk crystals to nanostructures and molecules[5,6]. During the last decades, since the isolation and characterization of graphene[14], large attention has been devoted to the study of 2D materials, due to their remarkable electronic and optical properties[15,16]. Since then, the GW approximation has been extensively applied to predict quasi-particle properties of these materials[17–27].

Often, 2D systems are treated using plane waves within the supercell approach, in which an amount of vacuum is added in the non periodic direction in order to remove spurious interactions among replicas. In principle, accurate GW calculations require the inclusion of a very large vacuum extension due to the long-range nature of the Coulomb interaction. This difficulty has been mitigated using truncated Coulomb potentials[28,29] that allows one to obtain converged results considering manageable inter-layer distances (e.g., in the range of 10–20 Å). Furthermore, characteristic properties of 2D screening, such as the dielectric function approaching unity in the long-wavelength limit (see below), are correctly reproduced in the supercell approach only if the potential is appropriately truncated[30,31]. However, once the Coulomb potential is truncated, the resulting sharp behaviour of the screened potential can make the integration over the Brillouin zone (BZ) rather inefficient[22,31]. Thus very large k-point grids are needed to obtain converged results, making the computation of quasiparticle (QP) properties within the GW method for 2D systems computationally expensive[32].

More in details, in a plane-wave basis set description, the screening properties are described by the matrix elements of the Fourier transform of the inverse dielectric function $\epsilon_{\mathbf{GG'}}^{-1}(\mathbf{q})$, where $\mathbf{G}$ is a reciprocal lattice vector and $\mathbf{q}$ a reciprocal vector of the first

BZ. In 2D systems, as already pointed out in the literature[30,33–37], the head [$\mathbf{G} = \mathbf{G'} = (0,0,0)$] of the dielectric matrix sharply approaches unity in the long wavelength limit (Fig. 1, left panel), and it is clear that with coarse meshes it is not possible to correctly reproduce such limit with a regular discretization procedure. In addition, the first matrix elements associated with lattice vectors along the confined direction ($\mathbf{G}_\perp$) show a dispersion in the long-wavelength limit, differently from the matrix elements with lattice vectors oriented in the periodic directions ($\mathbf{G}_\parallel$) which are approximately constant with respect to $|\mathbf{q}|$ (see Fig. 1). This trend originates from the fact that min $|\mathbf{G}_\perp|$ is significantly smaller than min $|\mathbf{G}_\parallel|$, due to the amount of vacuum added in the perpendicular direction. Furthermore, we note that in 2D systems the long-wavelength limit of the wing matrix of the dielectric matrix, $\epsilon_{\mathbf{G}0}^{-1}$, goes to zero as $|\mathbf{q}| \to 0$ (Fig. 1 right panel) leading to possible numerical instabilities when these terms are multiplied by the diverging Coulomb potential. All these features of the dielectric matrix contribute to slow the convergence of the QP properties with respect to the number of sampling points in the BZ, usually discretized on a uniform grid.

In the last years, different strategies have been proposed to accelerate the convergence of GW results for 2D systems with respect to the number of k-point sampling. Rasmussen et al.[35] proposed an analytic model for the long-wavelength limit of the head of the inverse dielectric function ϵ_{00}^{-1}. This model has been used to integrate the screened potential in a small region around the Γ point, thus reducing the size of the k-point mesh needed to converge the quasiparticle gap. However, denser meshes with respect to DFT are still required (e.g., for the band gap of MoS_2 converged results within 50meV were reported[35] using $18 \times 18 \times 1$ grids) as the analytic model is applied only to the $\mathbf{G} = \mathbf{G'} = 0$ matrix element.

Da Jornada et al.[36] proposed instead a fully numerical approach, where a nonuniform $\mathbf{q}$-sampling is used to increase the sampling close to the Γ point. This approach has been applied not only to the $\mathbf{G} = \mathbf{G'} = 0$ element of the dielectric matrix, but to a submatrix

---

[1]S3 Centre, Istituto Nanoscienze, CNR, Via Campi 213/a, Modena, Italy. [2]Present address: Dipartimento di Fisica, Università di Roma La Sapienza, Piazzale Aldo Moro 5, I-00185 Roma, Italy. ✉email: alberto.guandalini@uniroma1.it; pino.damico@nano.cnr.it; andrea.ferretti@nano.cnr.it; daniele.varsano@nano.cnr.it

npj
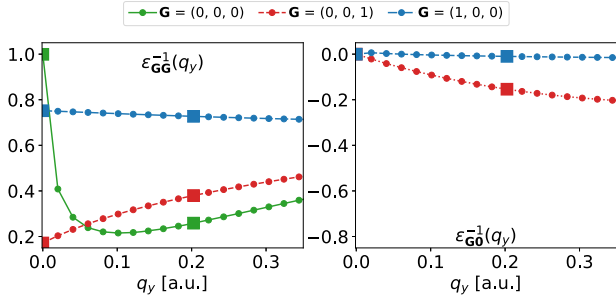
Fig. 1 Selected elements of the real part of the static inverse dielectric matrix of MoS₂. Diagonal and wing elements elements are plotted in the left and right panel respectively. Squares indicate values obtained with a $6 \times 6 \times 1$ grid, while dots with a $60 \times 60 \times 1$ grid.

($\mathbf{G}_\perp$, $\mathbf{G}'_\perp$) such that $|\mathbf{G}_\perp|,|\mathbf{G}'_\perp| < \min |\mathbf{G}_\parallel|$. In Xia et al.[38], the two previous strategies are combined by performing a non-uniform sub-sampling of the Brillouin zone around Γ followed by a non-linear fitting procedure to model the **q**-dependence of the self-energy terms (both exchange and correlation) instead of modelling the behaviour of the dielectric matrix or screened potential elements. Xing et al.[39] proposed a staggered mesh method for accelerating the BZ sampling convergence of the correlation energies evaluated with diagrammatic perturbation theory. While this work may be extended also for the calculation of QP corrections, to the best of our knowledge, it has not yet been applied in this context.

The methods of refs. [36,38] showed that meshes of size similar to those needed to converge the DFT ground state calculations were enough to obtain reliable results as demonstrated for the gap of MoSe₂ bilayer and MoS₂ monolayer. However, both methods rely on a nonuniform sampling, which add a convergence parameter to be managed (the number of sub-sampling points). Moreover, the region around Γ in which the additional sampling is performed (and consequently the nonlinear fitting in Xia et al.) depends on the size of the uniform grid. This may cause inconsistency problems when comparing results from different grids, e.g., in a convergence set of calculations, as increasing the grid region around Γ becomes smaller and smaller.

Motivated by these works, we show that the convergence of QP properties of 2D semiconductors with respect to the number of **k**-points in the BZ sampling can be accelerated, at the same level of previous methods found in the literature[36,38], by combining the Monte Carlo integration techniques with an interpolation scheme of the screened potential. Unlike the methods described above, the proposed method allows one to accelerate the convergence of the QP properties overcoming the need to rely on a nonuniform sampling. In addition, the same integration procedure (see below) is applied to the full BZ, thereby avoiding the need to treat the Γ region differently from the remaining part of the BZ. The proposed method has been implemented in the Yambo package[40,41].

The work is organized as follows: In "Methods", we present the main ideas of the proposed method and its implementation. In "Results", we show the performance of the method for three prototype 2D semiconductors: a transition metal dichalcogenide (MoS₂), a wide band gap insulator (hBN), and an anisotropic semiconductor (phosphorene). In section "Computational details", we provide the computational details, and in "Discussion", we draw the conclusions.

RESULTS

The W-av method

Within many-body perturbation theory, quasiparticle energies are usually calculated either by solving numerically the QP equation:

$$\varepsilon_{n\mathbf{k}}^{QP} = \varepsilon_{n\mathbf{k}}^{KS} + \langle n\mathbf{k}|\Sigma(\varepsilon_{n\mathbf{k}}^{QP}) - v_{xc}^{KS}|n\mathbf{k}\rangle, \qquad (1)$$

where $\{n\mathbf{k}\}$ are the KS wavefunctions and v_{xc}^{KS} is the exchange-correlation potential, or by linearizing the equation at the first order:

$$\varepsilon_{n\mathbf{k}}^{QP} = \varepsilon_{n\mathbf{k}}^{KS} + Z_{n\mathbf{k}}\langle n\mathbf{k}|\Sigma(\varepsilon_{n\mathbf{k}}^{KS}) - v_{xc}^{KS}|n\mathbf{k}\rangle, \qquad (2)$$

where the renormalization factor $Z_{n\mathbf{k}}$ is defined as:

$$Z_{n\mathbf{k}} = \left[1 - \langle n\mathbf{k}|\frac{\partial\Sigma(\omega)}{\partial\omega}|n\mathbf{k}\rangle\Big|_{\omega=\varepsilon_{n\mathbf{k}}^{KS}}\right]^{-1}. \qquad (3)$$

To obtain the QP correction of a single-particle state $|n\mathbf{k}\rangle$ in the GW approximation, we need to evaluate the diagonal matrix element of the self-energy,

$$\Sigma^{GW}(\omega) = -\int_{-\infty}^{+\infty}\frac{d\omega'}{2\pi i}e^{i\omega'0^+}, G(\omega+\omega')W(\omega'), \qquad (4)$$

where the screened interaction W is obtained from the expression $W(\omega) = v + v\chi(\omega)v = \varepsilon^{-1}(\omega)v$, with the reducible polarizability $\chi(\omega)$ treated at the RPA level. The self energy can be split into the exchange (x) and correlation (c) parts as

$$\langle n\mathbf{k}|\Sigma(\omega)|n\mathbf{k}\rangle \equiv \Sigma_{n\mathbf{k}}^x + \Sigma_{n\mathbf{k}}^c(\omega). \qquad (5)$$

Notably, both terms of the self-energy involve an integration over the momentum transfer **q**. If we discretize the BZ with a 2D uniform **k**-grid (centred at Γ), following the Monkhorst–Pack scheme[42], the momentum transfer **q** is discretized with the same uniform grid, and the **q** integrals can be evaluated as finite sums. Thus, the x self-energy is written as:

$$\Sigma_{n\mathbf{k}}^x = -\frac{1}{N_q\Omega}\sum_{v,\mathbf{q}}\sum_{\mathbf{G}}|\rho_{nv}(\mathbf{k},\mathbf{q},\mathbf{G})|^2 v_{\mathbf{G}}(\mathbf{q}), \qquad (6)$$

where Ω is the volume of the unit cell in real space, v labels the occupied bands, the ρ_{nm} matrix elements are defined as $\rho_{nm}(\mathbf{k},\mathbf{q},\mathbf{G}) = \langle n\mathbf{k}|e^{i(\mathbf{q}+\mathbf{G})\cdot\mathbf{r}}|m\mathbf{k}-\mathbf{q}\rangle$, and N_q is the number of points of the q grid. In order to eliminate periodic image interactions for a 2D system, we take the Coulomb potential in Eq. (6) as a truncated potential in a slab geometry. Its Fourier transform reads[28,29]:

$$v_{\mathbf{G}}(\mathbf{q}) = \frac{4\pi}{|\mathbf{q}+\mathbf{G}|^2}\left[1 - e^{-|\mathbf{q}_\parallel+\mathbf{G}_\parallel|L/2}\cos[(q_z+G_z)L/2]\right], \qquad (7)$$

where L is the length of the cell in the non-periodic z direction. As the q-grid is 2D, we have $q_z = 0$.

Nevertheless, Eq. (6) cannot be directly applied due to the divergence of the Coulomb interaction at $\mathbf{G} = \mathbf{q} = 0$. There are several approaches to treat such divergence[40,43–46]. Among these, we select the v-average (v-av) method (called random integration method and described in ref. [40]). In this method, it is assumed that the matrix elements $\rho_{nm}(\mathbf{k},\mathbf{q},\mathbf{G})$ are smooth with respect to **q**, and Eq. (6) is discretized in the following way

$$\Sigma_{n\mathbf{k}}^x = -\frac{1}{N_q\Omega}\sum_{v,\mathbf{q}}\sum_{\mathbf{G}}|\rho_{nv}(\mathbf{k},\mathbf{q},\mathbf{G})|^2 \bar{v}_{\mathbf{G}}(\mathbf{q}), \qquad (8)$$

where $\bar{v}$ is the average of the Coulomb interaction within a region of the BZ centred around **q** of the Monkhorst–Pack grid:

$$\bar{v}_{\mathbf{G}}(\mathbf{q}) = \frac{1}{D_\Gamma}\int_{D_\Gamma}d\mathbf{q}' v_{\mathbf{G}}(\mathbf{q}+\mathbf{q}'). \qquad (9)$$
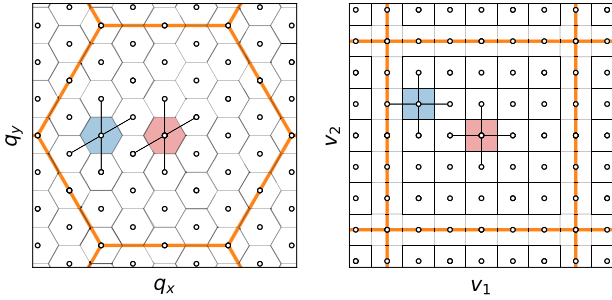
Fig. 2 Graphical representation of the 6 × 6 × 1 Monkhorst–Pack sampling of an hexagonal units cell. In the left panel, the reciprocal space is represented in cartesian coordinates ($\mathbf{q}$), in the right panel in reciprocal lattice coordinates ($\mathbf{v}$). A Monkhorst–Pack grid is always rectangular (or squared) in reciprocal lattice coordinates. The BZ in both representations are highlighted with thick orange lines. Smaller hexagons (squares) represent the mini-BZ of the q sampling in cartesian (reciprocal lattice) coordinates. The mini-BZ at Γ is highlighted in red, while an example at $\mathbf{q} \neq 0$ ($\mathbf{v} \neq 0$) in blue. Black lines connect the q point with its nearest neighbours in reciprocal lattice coordinates, which are used for the interpolation.

D_Γ is the small area of the Monkhorst–Pack grid centred around Γ (red area in Fig. 2). The integrals in Eq. (9) are evaluated via a 2D Monte Carlo technique.

In addition, Eq. (8), as compared with Eq. (6), leads to a faster convergence of the the exchange self-energy with respect to N_q, since Eq. (8) takes into account the variation of the bare potential within the region of the BZ centred around each $\mathbf{q}$ point and it has been extensively applied also to three dimensional semiconductors[47]. For practical purposes, it is sufficient to evaluate the averages up to a threshold $|\mathbf{G}|^2/2 < E_{cut}^{v-av}$, since the Coulomb interaction becomes a smooth function of $\mathbf{q}$ at large $|\mathbf{G}|$.

We now consider the correlation part of the self-energy, that is the most problematic term for 2D semiconductors. Within the plasmon-pole approximation (PPA) (we here adopt the Godby–Needs formulation[48]) the correlation part of the screened Coulomb potential, $W^c(\omega) = W(\omega) - v$, is written as:

$$W^c_{\mathbf{GG'}}(\mathbf{q}, \omega) = \frac{2R_{\mathbf{GG'}}(\mathbf{q})\Omega_{\mathbf{GG'}}(\mathbf{q})}{\omega^2 - [\Omega_{\mathbf{GG'}}(\mathbf{q}) - i\eta]^2}, \quad (10)$$

where the limit $\eta \to 0^+$ is implicitly assumed. Then, Σ^c can be expressed as:

$$\Sigma^c_{n\mathbf{k}}(\omega) = \frac{1}{N_q\Omega} \sum_{\mathbf{G},\mathbf{G'},\mathbf{q}} g^{n\mathbf{k}}_{\mathbf{GG'}}(\mathbf{q}, \omega) W^c_{\mathbf{GG'}}(\mathbf{q}), \quad (11)$$

where the matrix elements $g^{n\mathbf{k}}_{\mathbf{GG'}}$ are defined as:

$$g^{n\mathbf{k}}_{\mathbf{GG'}}(\mathbf{q}, \omega) = -\frac{1}{2}\sum_m$$
$$\times \frac{\rho_{nm}(\mathbf{k}, \mathbf{q}, \mathbf{G})\,\Omega_{\mathbf{GG'}}(\mathbf{q})\,\rho^*_{nm}(\mathbf{k}, \mathbf{q}, \mathbf{G'})}{\omega - \varepsilon^{KS}_{m\mathbf{k}-\mathbf{q}} + [\Omega_{\mathbf{GG'}}(\mathbf{q}) - i\eta]\,\mathrm{sgn}(\mu - \varepsilon^{KS}_{m\mathbf{k}-\mathbf{q}})}, \quad (12)$$

In Eq. (11) $W^c_{\mathbf{GG'}}(\mathbf{q})$ is the static component of the screened Coulomb interaction. In particular, $g^{n\mathbf{k}}_{\mathbf{GG'}}$ are smooth functions of $\mathbf{q}$ for ω far from $\Omega_{\mathbf{GG'}}$, where the PPA is justified.

For small $\mathbf{G}$ vectors, the correlation part of the screened potential, $W^c_{\mathbf{GG'}}(\mathbf{q})$ shows a sharp $\mathbf{q}$ dependence due to the behaviour of both the bare interaction $v_\mathbf{G}(\mathbf{q})$ and the inverse dielectric function $\epsilon^{-1}_{\mathbf{GG'}}(\mathbf{q})$, as shown in Fig. 1. For this reason, following a similar procedure already applied to $\Sigma^x_{n\mathbf{k}}$, we discretize Eq. (11) as

$$\Sigma^c_{n\mathbf{k}}(\omega) = \frac{1}{N_q\Omega} \sum_{\mathbf{G},\mathbf{G'},\mathbf{q}} g^{n\mathbf{k}}_{\mathbf{GG'}}(\mathbf{q}, \omega)\overline{W^c}_{\mathbf{GG'}}(\mathbf{q}), \quad (13)$$

where

$$\overline{W^c}_{\mathbf{GG'}}(\mathbf{q}) = \frac{1}{D_\Gamma}\int_{D_\Gamma} d\mathbf{q'} W^c_{\mathbf{GG'}}(\mathbf{q} + \mathbf{q'}) \quad (14)$$

is the average of the correlation part of the screened potential in the mini-BZ around $\mathbf{q}$ of the Monkhorst–Pack grid. The evaluation of the correlation part of the self-energy via Eq. (14) is referred to in the following as the W-av method. The integrals in Eq. (14) are calculated using a 2D Monte Carlo integration method, where $\overline{W^c}_{\mathbf{GG'}}(\mathbf{q} + \mathbf{q'})$ is evaluated considering typically $\approx 10^6 \mathbf{q'}$ points in the region around Γ (red area of Fig. 2) making use of an interpolation scheme, that is discussed in details in the next section. The number of random points used to evaluate the integrals guarantees a statistical error that does not interfere with the accuracy of the calculation. In practice, the Monte Carlo average is performed for a limited number of matrix elements of W such that $|\mathbf{G}|^2/2 < E_{cut}^{W-av}$, i.e., for the matrix elements presenting a sharp behaviour as a function of $\mathbf{q}$, while for the remaining $\mathbf{G}$ vectors the screening is evaluated on the $\mathbf{q}$ grid determined by the $\mathbf{k}$-point sampling.

Importantly, the W-average correction performed for $|\mathbf{G}|^2/2 < E_{cut}^{W-av}$ is applied to every $\mathbf{q}$ point of the BZ, at variance with other proposed methods where corrections are applied to the $\mathbf{q} = 0$ term only[35,36,38].

We note the W-av method, here derived along with the PPA, may be easily generalized to full-frequency treatments of the self-energy, by averaging the dynamical screened interaction, and not only its static part, with a generalized version of Eq. (14). However, this is out of the scope of this work.

Interpolation of the static screening
In this Section, we describe a procedure to interpolate the correlation part of the static screened potential $W^c_{\mathbf{GG'}}(\mathbf{q})$ as a function of $\mathbf{q}$, for the computation of the average $\overline{W^c}_{\mathbf{GG'}}$ according to Eq. (14). The head of the screened potential, W^c_{00}, can be exactly written as:

$$W^c_{00}(\mathbf{q}) = \frac{v_0(\mathbf{q})f(\mathbf{q})v_0(\mathbf{q})}{1 - v_0(\mathbf{q})f(\mathbf{q})}, \quad (15)$$

where $f(\mathbf{q})$ is an auxiliary function defined in the Supplementary Methods. The expression of Eq. (15) suggests that it is possible to use $f(\mathbf{q})$ for the interpolation of $W^c_{00}(\mathbf{q})$. In fact, while $W^c_{00}(\mathbf{q})$ shows a sharp behavour as a function of $\mathbf{q}$, the function $f(\mathbf{q})$ is smoother, as it resembles the irreducible response function $\chi^0_{00}(\mathbf{q})$ plus some corrections due to local-field contributions. In fact, $f(\mathbf{q}) = \chi^0_{00}(\mathbf{q})$ if local field effects are neglected. Guided by this argument, we propose to represent the matrix elements of the static screening as

$$W^c_{\mathbf{GG'}}(\mathbf{q} + \mathbf{q'})$$
$$= \frac{v_\mathbf{G}(\mathbf{q} + \mathbf{q'})f_{\mathbf{GG'}}(\mathbf{q} + \mathbf{q'})v_{\mathbf{G'}}(\mathbf{q} + \mathbf{q'})}{1 - \sqrt{v_\mathbf{G}(\mathbf{q} + \mathbf{q'})}f_{\mathbf{GG'}}(\mathbf{q} + \mathbf{q'})\sqrt{v_{\mathbf{G'}}(\mathbf{q} + \mathbf{q'})}}, \quad (16)$$

where the Coulomb interaction $v_\mathbf{G}$ is given by Eq. (7) and $f_{\mathbf{GG'}}$ is an auxiliary function. We note that Eq. (16) is the simplest generalization of Eq. (15) for the case $\mathbf{G} \neq 0$, $\mathbf{G'} \neq 0$. We remind that in our notation $\mathbf{q}$ is a point of the Monkhorst-Pack grid, while $\mathbf{q'}$ belongs to D_Γ (red region in Fig. 2). By inverting Eq. (16) on the $\mathbf{q}$-points of the mesh we have:

$$f_{\mathbf{GG'}}(\mathbf{q}) = \frac{W^c_{\mathbf{GG'}}(\mathbf{q})}{\sqrt{v_\mathbf{G}(\mathbf{q})}\sqrt{v_{\mathbf{G'}}(\mathbf{q})}}$$
$$\times \left[W^c_{\mathbf{GG}}(\mathbf{q}) + \sqrt{v_\mathbf{G}(\mathbf{q})}\sqrt{v_{\mathbf{G'}}(\mathbf{q})}\right]^{-1}. \quad (17)$$

In order to compute $f_{\mathbf{GG'}}(\mathbf{q} + \mathbf{q'})$ without requiring a dense mesh of $\mathbf{q}$ points, the function is numerically determined by interpolating between the given $\mathbf{q}$ point and its four nearest neighbours in reciprocal lattice coordinates $\mathbf{v}$. A sketch of the interpolation scheme is shown in Fig. 2.

The auxiliary function is parametrized as:

$$f_{\mathbf{GG'}}(\mathbf{v} + \mathbf{v'}) \equiv f_{\mathbf{GG'}}(\mathbf{v}) + \overline{f}_{\mathbf{GG'}}(\mathbf{v}) \cdot \mathbf{v'} \\ + \mathbf{v'} \cdot \overline{\overline{f}}_{\mathbf{GG'}}(\mathbf{v}) \cdot \mathbf{v'}, \tag{18}$$

where

$$\overline{f}_{\mathbf{GG'}}(\mathbf{v}) = \begin{bmatrix} f^1_{\mathbf{GG'}}(\mathbf{v}) & f^2_{\mathbf{GG'}}(\mathbf{v}) \end{bmatrix} \tag{19}$$

and,

$$\overline{\overline{f}}_{\mathbf{GG'}}(\mathbf{v}) = \begin{bmatrix} f^{11}_{\mathbf{GG'}}(\mathbf{v}) & f^{12}_{\mathbf{GG'}}(\mathbf{v}) \\ f^{21}_{\mathbf{GG'}}(\mathbf{v}) & f^{22}_{\mathbf{GG'}}(\mathbf{v}) \end{bmatrix}, \tag{20}$$

$\mathbf{v}$ and $\mathbf{v'}$ being $\mathbf{q}$ and $\mathbf{q'}$ in reciprocal lattice coordinates. The polynomial dependence of $f_{\mathbf{GG'}}(\mathbf{v} + \mathbf{v'})$ with respect to $\mathbf{v'}$ is inspired by the Taylor expansion of $f_{\mathbf{GG'}}$ around $\mathbf{v}$. In Eq. (18), there are six coefficients that must be determined. As there are only four nearest neighbours, thus four conditions to apply, we set for simplicity $f^{12}_{\mathbf{GG'}}(\mathbf{v}) = f^{21}_{\mathbf{GG'}}(\mathbf{v}) = 0$. This choice corresponds to adopt a bilinear interpolation.

We note that $f_{00}(\mathbf{q} \to 0)$ is the most relevant element in the integration of the self-energy[35]. For semiconductors, it is possible to exploit the known behaviour $\lim_{\mathbf{q} \to 0} f_{00}(\mathbf{q}) \propto |\mathbf{q}|^2$ (see Supplementary Methods and ref. [49]) to impose a specific and more accurate functional form to the head ($\mathbf{G} = 0$ and $\mathbf{G'} = 0$) at $\mathbf{q} = 0$. Following the model for the inverse dielectric function adopted by Ismail-Beigi[28] we consider for $f_{00}(\mathbf{v'})$ the expression:

$$f_{00}(\mathbf{v'}) \equiv \mathbf{q'} \cdot \overline{\overline{f}}_{\text{lim}} \cdot \mathbf{q'} e^{-\sqrt{\alpha^2 v_1'^2 + \beta^2 v_2'^2}}. \tag{21}$$

where $\overline{\overline{f}}_{\text{lim}}$ is a 2×2 tensor which describes the anisotropy of χ^0_{00} and of W^c_{00}, and $\mathbf{q'} = \mathbf{q'}(\mathbf{v'})$. We note that in Eq. (21) the $\overline{\overline{f}}_{\text{lim}}$ tensor is represented in cartesian coordinates. However, we stress that the representation basis is arbitrary, as the tensorial scalar product does not depend on the coordinate choice. This choice, differently from the reciprocal lattice unit representation, makes the $\overline{\overline{f}}_{\text{lim}}$ proportional to the identity matrix in the case of isotropic systems. We can partially account for the anisotropy of the auxiliary function by keeping the diagonal form ($f^{xy}_{\text{lim}} = f^{yx}_{\text{lim}} = 0$) but relaxing the proportionality to the identity matrix ($f^{xx}_{\text{lim}} \neq f^{yy}_{\text{lim}}$).

By substituting Eq. (21) into Eq. (17) and taking the $|\mathbf{q}| \to 0$ limit along the x and y directions, respectively (the periodic directions),

we have

$$\begin{cases} f^{xx}_{\text{lim}} = \frac{W^c_{00}(q'_x \to 0, q'_y = 0)}{(2\pi L)^2} \\ f^{yy}_{\text{lim}} = \frac{W^c_{00}(q'_x = 0, q'_y \to 0)}{(2\pi L)^2} \end{cases} \tag{22}$$

Otherwise, we may neglect the anisotropy of the auxiliary function adding the following approximation: $f^{xx}_{\text{lim}} \approx f^{yy}_{\text{lim}} \equiv f_{\text{lim}}$, where

$$f_{\text{lim}} = \frac{W^c_{00}(\mathbf{q'} \to 0)}{(2\pi L)^2}. \tag{23}$$

In Eq. (23), the limit is performed along the in-plane 110 cartesian direction, in order to partially average between the x and y directions. The α and β coefficients in Eq. (21) are obtained by interpolation, using the nearest neighbours of the $\mathbf{q} = 0$ point. We note there are only two independent nearest-neighbour conditions to be applied, due to the symmetry property $f_{00}(\mathbf{q}) = f_{00}(-\mathbf{q})$ [which can be derived from the symmetry property $\chi^0_{\mathbf{GG'}}(\mathbf{q}) = \chi^0_{-\mathbf{G'}-\mathbf{G}}(-\mathbf{q})$].

Accuracy of the interpolation

We now present the results obtained with the interpolation scheme derived in "Methods" for three prototype monolayer materials starting from the transition metal dicalcogenide MoS_2. Electronic properties of MoS_2 have been extensively studied in the literature, including several calculations using the G_0W_0 approach[31,34,50,51]. It is a direct gap material with hexagonal structure having the gap localized at the K/K' point in the BZ. The valence band at K/K' is split due to spin-orbit coupling[52], but since we are interested in the convergence behaviour with respect to the $\mathbf{q}$-point sampling, and for sake of simplicity, we have not included spin-orbit effects in the present calculations. In addition, MoS_2 has been used to test two other convergence-accelerator schemes[35,38], which allows for a direct comparison with our approach.

In Fig. 3, we show some matrix elements of the correlation part of the screened potential $W^c_{\mathbf{GG'}}(\mathbf{q})$ and the auxiliary function $f_{\mathbf{GG'}}$ [see Eq. (17)] as a function of the momentum transfer q. The interpolation functions (orange lines) are computed starting from the data on a coarse grid ($6 \times 6 \times 1$), and compared with the same quantities computed with a denser grid ($60 \times 60 \times 1$), taken here
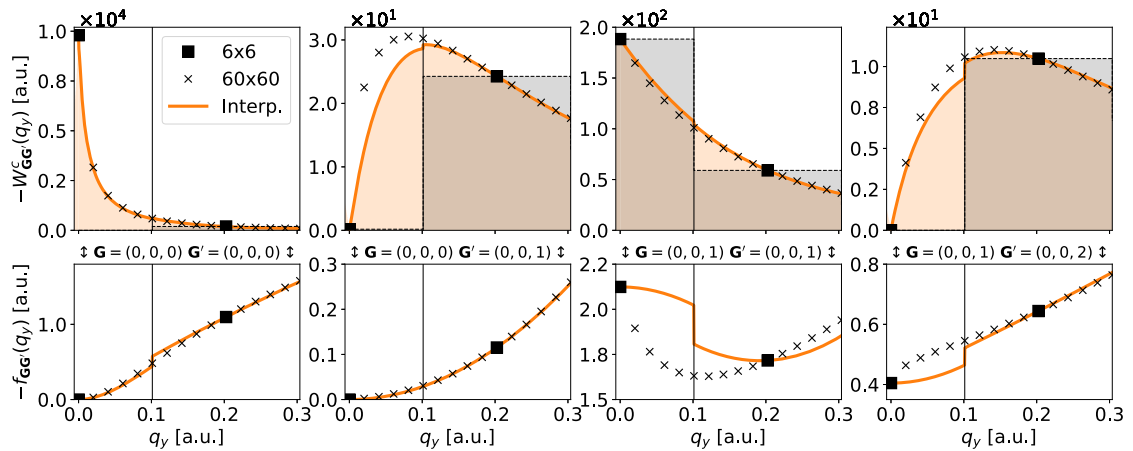
Fig. 3 Selected matrix elements of the correlation part of the screened potential (upper panels) and of the auxiliary function (lower panels) for the MoS_2 monolayer. Squares (crosses) are the numerical values obtained with a $6 \times 6 \times 1$ ($60 \times 60 \times 1$) Monkorst–Pack grid. The interpolated functions between the points of the coarser mesh are plot with orange lines. The grey-shaded areas represent the values of the integral of W^c when a simple trapezoidal rule is applied to the coarser grid (see the text for details about the missing contribution for $\mathbf{G} = \mathbf{G'} = 0$ and $q \approx 0$). The orange-shaded area represent the values of the integral of W^c obtained with the W-av method. Different domains of integration of the W-av method (which in 2D corresponds to the hexagons in the left panel of Fig. 2) are here separated with vertical black lines. We note the interpolation is discontinuous at the domain's border, as the interpolation procedure is applied at each domain separately. We remember that z here is the non-periodic direction. The auxiliary functions are multiplied by a factor 10^2 for clarity.

as a benchmark. The matrix element of W contributing the most to the GW correction is the $\mathbf{G} = \mathbf{G}' = 0$ term (Fig. 3 left panels), being $W_{\mathbf{GG}'}^c$ at least two order of magnitude larger than the other elements. As shown in Fig. 3, for the $\mathbf{G} = \mathbf{G}' = 0$ element there is a very good agreement between the results obtained interpolating the coarser grid (orange line) and the values calculated using the denser grid. For all the matrix elements considered, the auxiliary function $f_{\mathbf{GG}'}$ is smoother than $W_{\mathbf{GG}'}^c$ which supports the choice of interpolating $f_{\mathbf{GG}'}$ instead of $W_{\mathbf{GG}'}^c$. Fig. 3

shows no clear trend between the interpolation accuracy of $f_{\mathbf{GG}'}$ and of $W_{\mathbf{GG}'}^c$, in particular in the region $q \approx 0$. Since the different $\mathbf{G}$-components of the bare Coulomb potential, Eq. (7), have different limits and slopes for $|\mathbf{q}| \to 0$, the error associated with the interpolation of $f_{\mathbf{GG}'}$ can be both enhanced or quenched when propagated to $W_{\mathbf{GG}'}^c$. Despite this, we find a very good agreement between the interpolated values of $W_{\mathbf{GG}'}^c$ and the results obtained with the denser grid for all the considered matrix elements.

The grey shaded areas represent the integrals of $W_{\mathbf{GG}'}^c$ as obtained by applying the trapezoidal rule to the coarser grid together with the regularization of the Coulomb potential at $\mathbf{G} = \mathbf{G}' = \mathbf{q} = 0$, given by Eq. (9). For the sake of comparison, the same integrals, now obtained by using the interpolation, are highlighted in orange. The trapezoidal rule, due to the regularization of the bare Coulomb potential, misses completely the integral contribution at $\mathbf{G} = \mathbf{G}' = 0$ because of the vanishing value of $[\epsilon_{00}^{-1}(\mathbf{q} = 0) - 1]$, while $\bar{v}_0(\mathbf{q} = 0)$ remains finite.

Therefore, averaging the whole W^c, as we do in Eq. (14), instead of averaging v, Eq. (9), and multiplying by $[\epsilon_{00}^{-1}(\mathbf{q}) - 1]$, is mandatory to have a contribution different from zero in this region.

We also note that the trapezoidal rule misses the integral contributions of $W_{\mathbf{GG}'}^c$ for $\mathbf{G} = 0$ or $\mathbf{G}' = 0$ (wings) in the long-wavelength limit ($q \to 0$), since $W_{\mathbf{GG}'}^c(\mathbf{q}) \to 0$ as $q \to 0$. Finally, when $\mathbf{G}, \mathbf{G}' \neq 0$, the trapezoidal rule overestimate the integral in the region $q \approx 0$. The orange areas, obtained with the interpolation functions, give instead a good description of the areas under the dense grid data. This justifies the accuracy of the interpolation method with fairly coarse grids, as detailed in the following.

Convergence of the fundamental gap

In Fig. 4, we show the results for the QP band gap as a function of the $\mathbf{q}$-point sampling for MoS_2, hBN, and phosphorene. As for the case of MoS_2, also hBN[53–59] and phosphorene monolayer[23,60,61] have been extensively studied using GW approach. Moreover, due to its high anisotropy, the phosphorene monolayer is an ideal system to test the two proposed treatments of the $f_{\mathbf{GG}'}$ anisotropy, given in Eqs. (23) and (22).

In Fig. 4, the convergence of the fundamental gap for the three materials as a function of the $\mathbf{q}$-sampling is shown using the proposed accelerated method (W-av) and the v-av method. In the latter case, only the $\mathbf{q} = \mathbf{G} = 0$ term of the Coulomb interaction has been averaged, in order to regularize the Coulomb divergence. We verified that the use of the v-av method to treat the $\mathbf{q} \neq 0$ an $\mathbf{G} \neq 0$ terms of the Coulomb interaction does not significantly affect the results of the fundamental gap for the considered systems. The v-av method shows a very slow convergence with respect to N_k, as expected, and the gaps in the limit of an infinitely dense grids have been obtained by using an $1/N_k$ extrapolation. For all the three cases we note that the gap is overestimated when unconverged grids are used, mainly due to the lack of the long wavelength contributions of the correlation parts of the screened potential, as explained in the previous section (see Fig. 3). Using the v-av method, to obtain a gap value within less than ± 50 meV with respect to the extrapolated value, $\mathbf{k}$-grids of $54 \times 54 \times 1$, $36 \times 36 \times 1$, and $36 \times 50 \times 1$ are required for MoS_2, hBN, and phosphorene, respectively.
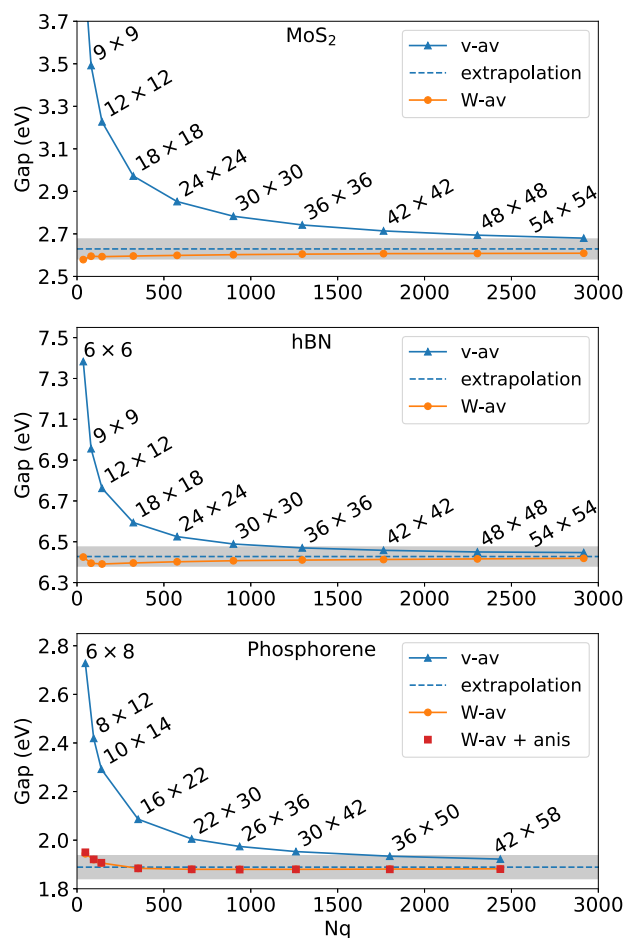
Fig. 4 Convergence of the quasiparticle band gap of MoS_2 (upper panel), hBN (middle panel), and phosphorene (lower panel) with respect to the number of sampling points of the BZ. Blue lines indicate results obtained with standard integration methods. The extrapolated values are indicated with an horizontal dashed line (see the text for more details about the extrapolation procedure). Orange lines are the results obtained with the W-av method. For the case of phosphorene, red squares indicate results obtained with the W-av method, in which the anisotropic behaviour of the screened potential is included through Eq. (23). The grey shaded regions show the converge tolerance (± 50 meV) and are centred at the extrapolated values.

With the proposed W-av method, the convergence of the gaps is greatly accelerated, and we obtain converged results already using $6 \times 6 \times 1$, $6 \times 6 \times 1$ and $8 \times 12 \times 1$ grids for MoS_2, hBN, and phosphorene, respectively, comparable with those required to obtain converged DFT results. These grids are respectively 80, 40 and 20 times smaller than the ones required to have similar accuracy without acceleration. As an example, the time-to-solution (on a single node) for the calculation of the converged GW energy gap in the case of MoS_2, reduces from about 11.5 h to less than a minute, thanks to the reduction of the mesh-size (from 54×54 to 6×6) obtained through the application of the W-av method. Converged results using similar size of $\mathbf{k}$-grids were also obtained with alternative accelerator schemes[36,38]. However, within the present method, differently from the other proposed strategies[36,38], no additional sub-sampling points are required to be computed in the region $q \approx 0$.

The orange dots in Fig. 4 are obtained with a parametrization of the head of the auxiliary function given by Eq. (23), which accounts for the anisotropy of the system by simply interpolating along the direction (110). Nevertheless, for phosphorene, that is
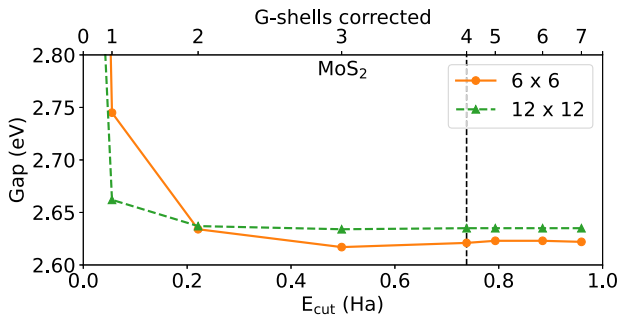
Fig. 5 Convergence of the quasiparticle band gap of MoS$_2$ obtained with the W-av method with respect to the cutoff energy of the correction. In the upper x-axis it is shown the numbers of G shells corrected. Orange (green) lines indicate results obtained with the $6 \times 6 \times 1$ ($12 \times 12 \times 1$) Monkorst–Pack grid. The vertical dashed line indicates the E_{cut}^{av} used in Fig. 4.

highly anisotropic, we have also taken explicitly into account the anisotropy of W^c, using a parametrization of the auxiliary function given by Eq. (22) (red dots). Although the long-wavelength limits of W_{00}^c are different, the average of the correlation part of the potential, see Eq. (14), is very similar in the two schemes and the resulting quasiparticle corrections do not show substantial differences. Despite the present results for phosphorene show that the explicit anisotropic treatment does not affect the value of the computed band gap, this does not exclude the fact that it can be potentially relevant for other systems and deserves further investigation.

Next, we turn the attention on the role of the number of matrix elements of $W_{GG'}^c(\mathbf{q})$ averaged through Eq. (14), identified by the parameter E_{cut}^{av}. In Fig. 5, we plot the convergence of the band gap of MoS$_2$ with respect to E_{cut}^{av}, or, alternatively, with respect to the number of $\mathbf{G}$ shells for which the averaging procedure is employed. In the plot, points at $E_{cut}^{av} = 0$ refer to gaps obtained with the v-av method, i.e., blue triangles shown in the top panel of Fig. 4. The W averaging of the first element gives the largest contribution to the convergence acceleration, closing the gap to 1.28 and 0.60 eV for the $6 \times 6 \times 1$ and $12 \times 12 \times 1$ grids, respectively. The W averaging of the first $\mathbf{G}_\perp$ matrix elements is also important to obtain converged results with coarser grids. By looking at Fig. 3, it is evident that the standard integration technique (black shaded area) misses the $\mathbf{q} = 0$ contribution of the wing elements, as $W_{0\mathbf{G}_\perp}^c(\mathbf{q} \to 0) = 0$. The W-av method (orange shaded area) provides instead a finite contribution, improving the convergence trend. In particular, the coarser the grid, the more important is the averaging of $W_{\mathbf{G}_\perp \mathbf{G}'}^c$, as shown by the comparison of the $6 \times 6 \times 1$ with the $12 \times 12 \times 1$ grids. Still, in both cases, the convergence is reached for a small number of G shells, which translates into a nearly negligible added computational cost required to perform the averaging of the screened potential. According to our results, $E_{cut}^{av} \approx 1$–2 Ry is a reasonable choice for all the systems considered.

Comparison with the literature

Finally, in Table 1, we show the G_0W_0 converged gaps of MoS$_2$, hBN, and phosphorene and compare them with the data present in the literature. We emphasize that the results presented in Table 1 have been obtained with an increased number of bands and cutoff energy of the dielectric function with respect to the data shown in the previous figures, as explained in detail in section "Computational details". The MoS$_2$ gaps found in the literature ranges from 2.41 to 2.78 eV. Our value, 2.62 eV, lies within this range. Instead, the fundamental gaps of hBN found in the literature differ considerably from each other, with discrepancies most likely due to the different approximations employed in the

Table 1. Converged G_0W_0 gaps of MoS$_2$, hBN, and phosphorene as obtained within our work and found in the literature.

	This work	Literature
	G_0W_0	G_0W_0
MoS$_2$	2.62	2.54[35], 2.77[31], 2.78[50]
		2.41[51], 2.56[38]
hBN	6.82	7.06[35], 7.32[53], 7.40[56], 6.00[58]
Phosphorene	2.04	2.03[35], 2.04[36], 1.56[64]
		2.07[62], 1.94[63]

calculations. Coming to the case of phosphorene, the gap computed within this work is generally in agreement with the results found in the literature.[35,36,62,63] Only the value found in ref. [64] deviates significantly from the others. Notably, in this work the fundamental gap of the periodic structure is obtained by extrapolating the thermodynamic limit from finite size systems of increasing size, at variance with the other works, where a periodic structure is considered. Such extrapolation procedure may be the cause of the observed discrepancy.

DISCUSSION

Accurate results for the calculation of quasiparticle energies in the GW approximation for 2D semiconductors can be obtained only by using very large $\mathbf{k}$-point grids, making calculations computationally very demanding. We have provided here a technique based on a stochastic averaging and interpolation of the screened potential to accelerate the convergence of the self energy with respect to the $\mathbf{q}$-point sampling. We have tested the proposed scheme for the calculation of the QP gap of three prototypical monolayer semiconductors: MoS$_2$, hBN, and phosphorene. We find that grids such as $6 \times 6 \times 1$, $6 \times 6 \times 1$ and $8 \times 12 \times 1$ are enough to obtain converged results for the fundamental gap up to 50 meV for MoS$_2$, hBN, and phosphorene, respectively. These grids are 80, 40 and 20 times smaller than those required to achieve a similar accuracy when averaging only the bare coulomb potential (v-av method). Taking the $\mathbf{k}$ and $\mathbf{q}$ grids to be identical, G_0W_0 typically scales[65] as N_k^2. When this is the case, with the proposed method the computational cost of a G_0W_0 calculation is reduced by at least two orders of magnitude, without loss of accuracy. The proposed W-av method is able to describe the anisotropy of the screened potential at different levels of approximations, and differently from other methods recently proposed does not rely on any sub-sampling of the BZ.

The possibility to extend the present methodology to metals and systems with different dimensionalities (1D or 3D) is envisaged and will be explored in a future research.

METHODS

Computational details

DFT calculations were performed using a plane wave basis set as implemented in the Quantum ESPRESSO package[66], and using the Perdew-Burke-Ernzerhof (PBE) exchange-correlation functional[67]. We have considered supercells with an interlayer distance $L = 10$ Å for MoS$_2$ and $L = 15$ Å for hBN and phosphorene, which are enough to obtain converged results with respect to the cell size, in agreement with ref. [35]. The kinetic energy cutoff for the wavefunctions was set to 60 Ry and we adopted norm-conserving pseudopotentials to model the electron-ion interaction.

G_0W_0 calculations were performed with the Yambo package[40,41]. In the calculations reported in Figs. 1, 3–5, we used a cutoff of 5 Ry for the size of the dielectric matrix, including up to 400 states in the sum-over-state of the response function. The

same number of states has been employed in the calculation of the correlation part of the self energy. To accelerate the convergence with respect to the number of empty states we have used the algorithm described in refs. [41,68]. Despite the cutoff used to represent the dielectric matrix is not enough to provide highly converged QP properties, it is sufficient to provide accurate convergence trends with respect to the **q**-sampling. In the calculations reported in Table 1, we included up to 600 states for MoS_2 and phosphorene, while 1200 for hBN, both in the response function and in the Green's function, with a size of the dielectric matrix of 25 Ry. We employed **k**-point grids of $9 \times 9 \times 1$, $12 \times 12 \times 1$, and $10 \times 14 \times 1$ for MoS_2, hBN and phosphorene, respectively.

DATA AVAILABILITY

CODE AVAILABILITY

The code developed in this work is available since the 5.1 version of the Yambo package.

REFERENCES

1. Hedin, L. New method for calculating the one-particle green's function with application to the electron-gas problem. *Phys. Rev.* **139**, A796–A823 (1965).
2. Strinati, G., Mattausch, H. J. & Hanke, W. Dynamical aspects of correlation corrections in a covalent crystal. *Phys. Rev. B* **25**, 2867–2888 (1982).
3. Hybertsen, M. S. & Louie, S. G. Electron correlation in semiconductors and insulators: band gaps and quasiparticle energies. *Phys. Rev. B* **34**, 5390–5413 (1986).
4. Godby, R. W., Schlüter, M. & Sham, L. J. Self-energy operators and exchange-correlation potentials in semiconductors. *Phys. Rev. B* **37**, 10159–10175 (1988).
5. Reining, L. The gw approximation: content, successes, and limitations. *Wiley Interdiscip. Rev. Comput. Mol. Sci.* **8**, e1344 (2018).
6. Golze, D., Dvorak, M. & Rinke, P. The gw compendium: a practical guide to theoretical photoemission spectroscopy. *Front. Chem.* **7**, 377 (2019).
7. Marzari, N., Ferretti, A. & Wolverton, C. Electronic-structure methods for materials design. *Nat. Mater.* **20**, 736–749 (2021).
8. Damascelli, A., Hussain, Z. & Shen, Z.-X. Angle-resolved photoemission studies of the cuprate superconductors. *Rev. Mod. Phys.* **75**, 473–541 (2003).
9. Guzzo, M. et al. Valence electron photoemission spectrum of semiconductors: ab initio description of multiple satellites. *Phys. Rev. Lett.* **107**, 166401 (2011).
10. Caruso, F., Verdi, C., Poncé, S. & Giustino, F. Electron-plasmon and electron-phonon satellites in the angle-resolved photoelectron spectra of n-doped anatase TiO_2. *Phys. Rev. B* **97**, 165113 (2018).
11. Marini, A., Del Sole, R., Rubio, A. & Onida, G. Quasiparticle band-structure effects on the d hole lifetimes of copper within the gw approximation. *Phys. Rev. B* **66**, 161104 (2002).
12. Bechstedt, F., Fiedler, M., Kress, C. & Del Sole, R. Dynamical screening and quasiparticle spectral functions for nonmetals. *Phys. Rev. B* **49**, 7357–7362 (1994).
13. Zhou, J. S. et al. Unraveling intrinsic correlation effects with angle-resolved photoemission spectroscopy. *Proc. Natl Acad. Sci. USA* **117**, 28596–28602 (2020).
14. Geim, A. K. & Novoselov, K. S. *Nanoscience and Technology: A Collection of Reviews from Nature Journals* 11–19 (World Scientific, 2010).
15. Ferrari, A. C. et al. Science and technology roadmap for graphene, related two-dimensional crystals, and hybrid systems. *Nanoscale* **7**, 4598–4810 (2015).
16. Bhimanapati, G. R. et al. Recent advances in two-dimensional materials beyond graphene. *ACS Nano* **9**, 11509–11539 (2015).
17. Trevisanutto, P. E., Giorgetti, C., Reining, L., Ladisa, M. & Olevano, V. Ab initio g w many-body effects in graphene. *Phys. Rev. Lett.* **101**, 226405 (2008).
18. Haastrup, S. et al. The computational 2d materials database: high-throughput modeling and discovery of atomically thin crystals. *2D Materials* **5**, 042002 (2018).
19. Rasmussen, A., Deilmann, T. & Thygesen, K. S. Towards fully automated gw band structure calculations: What we can learn from 60.000 self-energy evaluations. *npj Comput. Mater.* **7**, 1–9 (2021).
20. Qian, X., Liu, J., Fu, L. & Li, J. Quantum spin hall effect in two-dimensional transition metal dichalcogenides. *Science* **346**, 1344–1347 (2014).
21. Varsano, D., Palummo, M., Molinari, E. & Rontani, M. A monolayer transition-metal dichalcogenide as a topological excitonic insulator. *Nat. Nanotechnol.* **15**, 367–372 (2020).
22. Qiu, D. Y., Felipe, H. & Louie, S. G. Screening and many-body effects in two-dimensional crystals: monolayer MoS_2. *Phys. Rev. B* **93**, 235435 (2016).
23. Qiu, D. Y., da Jornada, F. H. & Louie, S. G. Environmental screening effects in 2d materials: renormalization of the bandgap, electronic structure, and optical spectra of few-layer black phosphorus. *Nano Lett.* **17**, 4706–4712 (2017).
24. da Jornada, F. H., Xian, L., Rubio, A. & Louie, S. G. Universal slow plasmons and giant field enhancement in atomically thin quasi-two-dimensional metals. *Nat. Commun* **11**, 1–10 (2020).
25. Wu, Y. et al. Quasiparticle electronic structure of honeycomb c3n: from monolayer to bulk. *2D Materials* **6**, 015018 (2018).
26. Zhang, Y., Xia, W., Wu, Y. & Zhang, P. Prediction of mxene based 2d tunable band gap semiconductors: Gw quasiparticle calculations. *Nanoscale* **11**, 3993–4000 (2019).
27. Qiu, D. Y., Coh, S., Cohen, M. L. & Louie, S. G. Comparison of gw band structure to semiempirical approach for an fese monolayer. *Phys. Rev. B* **101**, 235154 (2020).
28. Ismail-Beigi, S. Truncation of periodic image interactions for confined systems. *Phys. Rev. B* **73**, 233103 (2006).
29. Rozzi, C. A., Varsano, D., Marini, A., Gross, E. K. U. & Rubio, A. Exact coulomb cutoff technique for supercell calculations. *Phys. Rev. B* **73**, 205119 (2006).
30. Cudazzo, P., Tokatly, I. V. & Rubio, A. Dielectric screening in two-dimensional insulators: Implications for excitonic and impurity states in graphane. *Phys. Rev. B* **84**, 085406 (2011).
31. Hüser, F., Olsen, T. & Thygesen, K. S. How dielectric screening in two-dimensional crystals affects the convergence of excited-state calculations: monolayer MoS_2. *Phys. Rev. B* **88**, 245309 (2013).
32. Thygesen, K. S. Calculating excitons, plasmons, and quasiparticles in 2d materials and van der Waals heterostructures. *2D Mater.* **4**, 022004 (2017).
33. Hüser, F., Olsen, T. & Thygesen, K. S. How dielectric screening in two-dimensional crystals affects the convergence of excited-state calculations: monolayer MoS_2. *Phys. Rev. B* **88**, 245309 (2013).
34. Qiu, D. Y., da Jornada, F. H. & Louie, S. G. Screening and many-body effects in two-dimensional crystals: monolayer MoS_2. *Phys. Rev. B* **93**, 235435 (2016).
35. Rasmussen, F. A., Schmidt, P. S., Winther, K. T. & Thygesen, K. S. Efficient many-body calculations for two-dimensional materials using exact limits for the screened potential: Band gaps of MoS_2, h-bn, and phosphorene. *Phys. Rev. B* **94**, 155406 (2016).
36. da Jornada, F. H., Qiu, D. Y. & Louie, S. G. Nonuniform sampling schemes of the Brillouin zone for many-electron perturbation-theory calculations in reduced dimensionality. *Phys. Rev. B* **95**, 035109 (2017).
37. Chernikov, A. et al. Exciton binding energy and nonhydrogenic rydberg series in monolayer Ws_2. *Phys. Rev. Lett.* **113**, 076802 (2014).
38. Xia, W. et al. Combined subsampling and analytical integration for efficient large-scale gw calculations for 2d systems. *npj Comput. Mater.* **6**, 118 (2020).
39. Xing, X. & Lin, L. Staggered mesh method for correlation energy calculations of solids: random phase approximation in direct ring coupled cluster doubles and adiabatic connection formalisms. *J. Chem. Theory Comput.* **18**, 763–775 (2022).
40. Marini, A., Hogan, C., Grüning, M. & Varsano, D. Yambo: an ab initio tool for excited state calculations. *Comput. Phys. Commun.* **180**, 1392–1403 (2009).
41. Sangalli, D. et al. Many-body perturbation theory calculations using the Yambo code. *J. Phys.: Condens. Matter* **31**, 325902 (2019).
42. Monkhorst, H. J. & Pack, J. D. Special points for Brillouin-zone integrations. *Phys. Rev. B* **13**, 5188–5192 (1976).
43. Gygi, F. & Baldereschi, A. Self-consistent hartree-fock and screened-exchange calculations in solids: application to silicon. *Phys. Rev. B* **34**, 4405–4408 (1986).
44. Carrier, P., Rohra, S. & Görling, A. General treatment of the singularities in Hartree–Fock and exact-exchange Kohn–Sham methods for solids. *Phys. Rev. B* **75**, 205126 (2007).
45. Deslippe, J. et al. Berkeleygw: a massively parallel computer package for the calculation of the quasiparticle and optical properties of materials and nanostructures. *Comput. Phys. Commun.* **183**, 1269–1289 (2012).
46. Pulci, O., Onida, G., Del Sole, R. & Reining, L. Ab initio calculation of self-energy effects on optical properties of gas (110). *Phys. Rev. Lett.* **81**, 5374 (1998).
47. Rangel, T. et al. Reproducibility in g0w0 calculations for solids. *Comput. Phys. Commun.* **255**, 107242 (2020).
48. Godby, R. W. & Needs, R. J. Metal-insulator transition in Kohn–Sham theory and quasiparticle theory. *Phys. Rev. Lett.* **62**, 1169–1172 (1989).
49. Pick, R. M., Cohen, M. H. & Martin, R. M. Microscopic theory of force constants in the adiabatic approximation. *Phys. Rev. B* **1**, 910–920 (1970).
50. Qiu, D. Y., da Jornada, F. H. & Louie, S. G. Optical spectrum of MoS_2: many-body effects and diversity of exciton states. *Phys. Rev. Lett.* **111**, 216805 (2013).

51. Molina-Sánchez, A., Sangalli, D., Hummer, K., Marini, A. & Wirtz, L. Effect of spin–orbit interaction on the optical spectra of single-layer, double-layer, and bulk MoS_2. *Phys. Rev. B* **88**, 045412 (2013).

52. Zhu, Z. Y., Cheng, Y. C. & Schwingenschlögl, U. Giant spin–orbit-induced spin splitting in two-dimensional transition-metal dichalcogenide semiconductors. *Phys. Rev. B* **84**, 153402 (2011).

53. Ferreira, F., Chaves, A. J., Peres, N. M. R. & Ribeiro, R. M. Excitons in hexagonal boron nitride single-layer: a new platform for polaritonics in the ultraviolet. *J. Opt. Soc. Am. B* **36**, 674–683 (2019).

54. Cudazzo, P. et al. Exciton band structure in two-dimensional materials. *Phys. Rev. Lett.* **116**, 066803 (2016).

55. Galvani, T. et al. Excitons in boron nitride single layer. *Phys. Rev. B* **94**, 125303 (2016).

56. Berseneva, N., Gulans, A., Krasheninnikov, A. V. & Nieminen, R. M. Electronic structure of boron nitride sheets doped with carbon from first-principles calculations. *Phys. Rev. B* **87**, 035404 (2013).

57. Şahin, H. et al. Monolayer honeycomb structures of group-iv elements and iii-v binary compounds: first-principles calculations. *Phys. Rev. B* **80**, 155453 (2009).

58. Blase, X., Rubio, A., Louie, S. G. & Cohen, M. L. Quasiparticle band structure of bulk hexagonal boron nitride and related systems. *Phys. Rev. B* **51**, 6868–6875 (1995).

59. Wirtz, L., Marini, A. & Rubio, A. Excitons in boron nitride nanotubes: dimensionality effects. *Phys. Rev. Lett.* **96**, 126104 (2006).

60. Li, L. et al. Direct observation of the layer-dependent electronic structure in phosphorene. *Nat. Nanotechnol.* **12**, 21–25 (2017).

61. Yoon, S. et al. Electrical control of anisotropic and tightly bound excitons in bilayer phosphorene. *Phys. Rev. B* **103**, L041407 (2021).

62. Brooks, J., Weng, G., Taylor, S. & Vlcek, V. Stochastic many-body perturbation theory for moiré states in twisted bilayer phosphorene. *J. Phys.: Condensed Matter* **32**, 234001 (2020).

63. Liang, L. et al. Electronic bandgap and edge reconstruction in phosphorene materials. *Nano Lett.* **14**, 6400–6406 (2014).

64. Wilhelm, J., Seewald, P. & Golze, D. Low-scaling gw with benchmark accuracy and application to phosphorene nanosheets. *J. Chem. Theory Comput.* **17**, 1662–1677 (2021).

65. Martin, R. M., Reining, L. & Ceperley, D. M. *Interacting Electrons: Theory and Computational Approaches* (Cambridge University Press, 2016).

66. Giannozzi, P. et al. Quantum espresso toward the exascale. *J. Chem. Phys.* **152**, 154105 (2020).

67. Perdew, J. P., Burke, K. & Ernzerhof, M. Generalized gradient approximation made simple. *Phys. Rev. Lett.* **77**, 3865–3868 (1996).

68. Bruneval, F. & Gonze, X. Accurate gw self-energies in a plane-wave basis using only a few empty states: towards large systems. *Phys. Rev. B* **78**, 085125 (2008).

AUTHOR CONTRIBUTIONS

A.G. implemented the method and performed the calculations. A.F., P.D.'A., and D.V. conceived the original idea of the work. All authors contributed to the method development, analysis of the results, wrote the manuscript, and critically discussed the paper.

COMPETING INTERESTS

The authors declare no competing interests.

ADDITIONAL INFORMATION

Supplementary information The online version contains supplementary material available at https://doi.org/10.1038/s41524-023-00989-7.

Correspondence and requests for materials should be addressed to Alberto Guandalini, Pino D'Amico, Andrea Ferretti or Daniele Varsano.

Reprints and permission information is available at http://www.nature.com/reprints

Publisher's note Springer Nature remains neutral with regard to jurisdictional claims in published maps and institutional affiliations.